

# Observational Signatures of Galactic Turbulent Dynamos

Yann Carteret<sup>1\*</sup>, Abhijit B. Bendre<sup>1</sup>, and Jennifer Schober<sup>1</sup>

<sup>1</sup>*Laboratoire d'Astrophysique, EPFL, CH-1290 Sauverny, Switzerland*

Accepted XXX. Received YYY; in original form ZZZ

## ABSTRACT

We analyse the observational signatures of galactic magnetic fields that are self-consistently generated in magnetohydrodynamic simulations of the interstellar medium through turbulence driven by supernova (SN) explosions and differential rotation. In particular, we study the time evolution of the Faraday rotation measure (RM), synchrotron radiation, and Stokes parameters by characterising the typical structures formed in the plane of observation. We do this by defining two distinct models for both thermal and cosmic ray (CR) electron distributions. Our results indicate that the maps of RM have structures which are sheared and rendered anisotropically by differential rotation and that they depend on the choice of the thermal electrons model as well as the SN rate. Synchrotron maps are qualitatively similar to the maps of the mean magnetic field along the line of sight and structures are only marginally affected by the CR model. Stokes parameters and related quantities, such as the degree of linear polarisation, are highly dependent on both frequency and resolution of the observation.

**Key words:** ISM: magnetic fields – radio continuum: ISM – galaxies: ISM – galaxies: magnetic fields – (magnetohydrodynamics) MHD – methods: data analysis

## 1 INTRODUCTION

Observations of the polarised radio synchrotron radiation The polarised radio synchrotron radiation emitted from the interstellar medium (ISM) of nearby disc galaxies and its associated Faraday rotation probe the topology and strength of the magnetic field hosted by them. The strength of the component along the line of sight (LOS) of the observer is estimated from the Faraday rotation measure (RM), while from the intensity of the radiation and its angle of polarisation the strength of the planar field component could be inferred (e.g. Beck & Wiełebinski 2013, and references therein). As such, it has been established that regular magnetic fields of kilo-parsec scales in coherence as well as the irregular or small-scale magnetic fields are abundantly present in nearby (e.g. Sofue et al. 1986; Thompson et al. 2006; Krause 2008; Fletcher 2010) and also in high-redshift disc galaxies (e.g. Bernet et al. 2008). Typical strengths of these fields are about a few tens of a  $\mu\text{G}$  in Milky Way like galaxies (Beck 2004), which corresponds to approximate equipartition between magnetic and turbulent kinetic energy.

The mechanism of the growth and sustenance of large-scale magnetic fields in galaxies, although unclear, is very likely a turbulent dynamo, operating in their ISM, as a result of an induction effect generated from a combined action of supernova (SN) driven turbulence, differential rotation, and density stratification (Rädler 1969; Parker 1971; Krause & Raedler 1980; Zeldovich et al. 1990; Brandenburg & Subramanian 2005). This process explains the amplification of very weak initial fields (which might have been generated in the early Universe (Kandus et al. 2011; Subramanian 2016) or through astrophysical mechanisms (Biermann 1950; Subramanian et al. 1994;

Kulsrud et al. 1997)) to a strength roughly in equipartition with the turbulent kinetic energy density. It has also been demonstrated in several empirical studies (see e.g. Shukurov et al. 2006, and references therein) through turbulent transport mechanisms, as well as in direct numerical studies with varying setups (see e.g. Gressel et al. 2008; Hanasz et al. 2009; Gent et al. 2013, etc.).

A better understanding of cosmic magnetic fields and mechanisms of their origin would enhance a general comprehension in numerous domains of astrophysics as they are believed to play an important role for example in the angular momentum transport in accretion discs (Shakura & Sunyaev 1973), in the morphology of the ISM and the star formation process (Price et al. 2009; Krumholz & Federrath 2019), and also in the propagation of cosmic rays (Yan & Lazarian 2008). Probing the observational signatures of the dynamo mechanism and being able to distinguish between various scenarios of generating the galactic magnetic field is therefore an important open problem. Scenarios of magnetic field evolution include different kinds of dynamos, like the small-scale or fluctuation dynamo which is fast but only produces magnetic fields on length scales smaller than the injection scales, the large-scale or mean-field dynamo, and combinations of the two.

Complications in observing cosmic magnetism arise primarily because the observables depend not only upon the field itself but also on the spatial distribution of thermal and non-thermal electrons, as well as on their statistical correlations with the magnetic field, which are usually not well understood. Typically observational studies of galactic magnetic fields rely upon theoretically inferred models of these distributions, and it is thus important to understand the extent to which these observational inferences depend upon the models of electron distributions.

In the current study, we address the aforementioned issue and

\* E-mail: yann.carteret@gmail.com

estimate observables associated with galactic magnetic fields from numerical simulations of the mean-field dynamo with the goal of improving the interpretation of observations of real galaxies. Similar synthetic observational analyses have been performed for interpreting the magnetic fields in the young galaxies (Bhat & Subramanian 2013; Sur et al. 2018), and also for the simulations of clusters of galaxies (Sur et al. 2021), where the small-scale or fluctuation dynamo is thought to be the prevalent mechanism for field generation (Schober et al. 2013). In the present analysis we focus on the ISM magnetic fields generated as a result of a large-scale dynamo.

We base this study on the data of the MHD simulations of galactic ISM performed by Bendre et al. (2015), the relevant details of which are also described in the following section. We process this data to perform a series of synthetic radio observations, and use physically motivated models for the distributions of thermal and CR electrons which are also crucial for modelling the continuum radio emission spectrum. We further explore the dependence of its polarisation angle, the two point correlation function of radio emission etc. upon these distributions. In Rappaz et al. (2022), a similar analysis of ISM simulations has been presented. These were also based on the MHD simulations of a local patch of galactic ISM, stirred with SN driven turbulence, which focused on realistically simulating the multi-phase morphology of ISM along with a detailed chemical network, and not specifically on the dynamo mechanism itself. The distribution of magnetic fields in these simulations therefore was a result of asymptotic turbulent decay of initially imposed uniform magnetic field. The simulations that we use here however, were focused on self consistently generating the large-scale dynamo effect from direct simulations of SN driven turbulence and differential shear.

The paper is organised as follows: In Sec. 2 we summarise the basic setup and the key results of the galactic dynamo simulations. In Sec. 3, we will present the post-processing of the simulations that allows us to extract various mock observables. Telescope effects will be discussed in Sec. 4. In Sec. 5 we comment on our different assumptions and we draw our conclusions in Sec. 6.

## 2 SIMULATIONS

In this section we briefly describe the setup of the direct numerical simulations (DNS) we analyse in the following sections. Detailed discussion of the DNS setup and its various outcomes are also presented in Bendre et al. (2015).

These were non-ideal MHD simulations of a local box of the ISM in a typical spiral galaxy, performed using NIRVANA MHD (Ziegler 2004) code. The simulation domain spanned  $\sim 0.8$  kpc by  $0.8$  kpc range in radial ( $x$ ) and azimuthal ( $y$ ) directions, while in the vertical  $z$  direction it spanned  $\sim -2.1$  to  $2.1$  kpc above and below the galactic mid-plane. The domain was resolved in  $96 \times 96 \times 512$  cells amounting to an uniform Cartesian grid with a resolution of  $\delta \sim 8$  pc. Shearing periodic boundary conditions were used at the radial while periodic ones were used at the  $y$  boundaries, to simulate respectively the radial shear and axisymmetry of azimuthal galactic flows. A flat rotation curve of galactic rotation was also included by letting the angular velocity decrease with radius  $R$  as  $\Omega \propto 1/R$ , with  $\Omega_0 = 100$  km  $s^{-1}$  kpc $^{-1}$  at the centre of the domain. The simulated ISM was composed only of hydrogen, although its multi-phase morphology was still captured in a rudimentary way by incorporating the temperature dependent rates of heat transfer, representing a piece-wise power law of radiative cooling (similar to Sánchez-Salcedo et al. 2002). The initial mass density  $\rho$  was vertically stratified and balanced hydro-

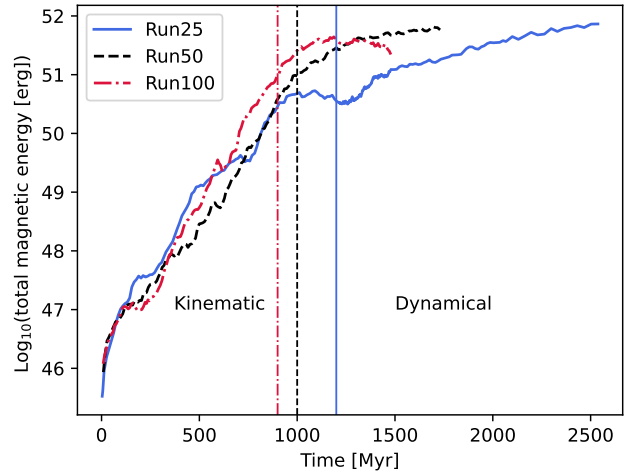


**Figure 1.** Time evolution of the magnetic field energy for the three runs. The thin vertical lines indicate the transition from the kinematic to the dynamical dynamo phase for the different runs.

statically with gravity. It had a scale height of  $\sim 300$  pc (and midplane value of  $\sim 10^{-24}$  g  $cm^{-2}$ ). Outflow boundary conditions were used at the vertical boundaries which allowed the outflow of the matter but restricted its inflow. SN explosions were simulated as spontaneous local expulsions of thermal energy injected at random locations scaling with the density and at predefined rates of 25%, 50%, and 100% of the average Milky Way SN rate ( $\sim 30$  Myr $^{-1}$  kpc $^{-2}$ , e.g., Ferrière 2001). We analyse all of these three models and refer to these as Run25, Run50, and Run100 respectively in the following sections.

This setup led to a quasi steady state of kinetic and thermal energies in all models within first few Myr, and the ISM segregated into multiple phases such as cold dense clouds in the midplane, the warm ionised phase, and hot ISM bubble in the outer halo of the galaxy. Magnetic energy, on the other hand amplified exponentially for about a Gyr, until it reached an approximate equipartition with respect to the turbulent kinetic energy, and thereafter it either saturated or kept on amplifying at a drastically slower growth rate (depending on the SN rate, see Fig. 1). We refer to these phases as kinematic and dynamical phase respectively in the following sections. Large-scale magnetic fields of strengths  $1 - 3 \mu$  G and of scale-heights  $\sim 500 - 800$  pc were also generated in all models, which have previously been analysed and explained as self consistent solutions of the mean field dynamo (Bendre et al. 2015). In Fig. 1 we illustrate the two different regimes of the dynamo regarding the magnetic energy growth, and in Fig. 2 we show the average along the  $z$  axis of the total magnetic field map in the  $x - y$  plane, taken in the dynamical phase (at  $T \approx 1508$  Myr) for Run25 as a comparison for the observables that we will present later.

## 3 OBSERVABLES

In this section we summarise the main results of our analysis, describe how they are obtained, as well as the assumptions involved.

### 3.1 Rotation measure and Faraday depth

Any linearly polarised signal can be decomposed into two circularly polarised components with opposite handedness. Under the effect of a

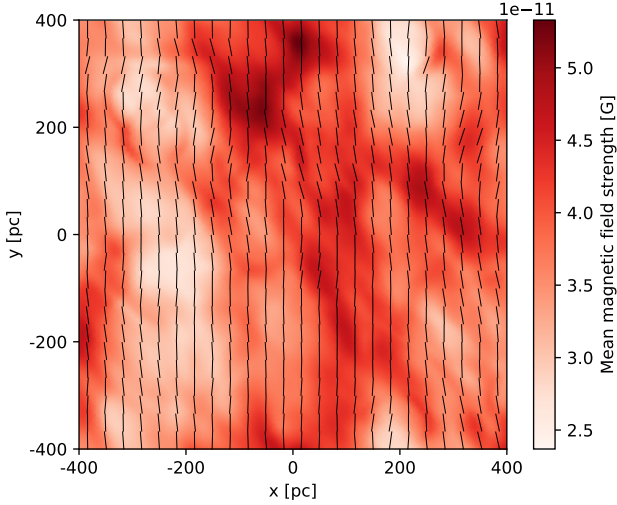


**Figure 2.** Total magnetic field strength averaged along the  $z$  axis for Run25 at  $T \approx 1508$  Myr. Black lines denote the orientation of the projected mean magnetic field in the  $x - y$  plane.

magnetic field, these two components accumulate a phase difference and difference in group velocities leading to a rotation of the plane of polarisation. This is known as Faraday rotation, and is characterised in the context of ISM by the strength of the component of magnetic field parallel to the wave vector, wavelength of the radiation, and density of scattering thermal electrons. The projected polarisation angle on the plane of observation is given by

$$\theta = \theta_0 + \lambda^2 \text{FD}, \quad (1)$$

where  $\theta_0$  is the initial angle,  $\lambda$  the wavelength of the photon and FD is the Faraday depth which is defined by [Burn \(1966\)](#) as

$$\text{FD} = K \int n_e \mathbf{B} \cdot d\mathbf{l}, \quad (2)$$

where the integration is along the line of sight (LOS) from the source to the observer.  $K$  depends upon the natural constants as  $K = e^3 / (2\pi m_e^2 c^4) \approx 0.812 \text{ rad m}^{-2} \text{ cm}^3 \mu\text{G}^{-1} \text{ pc}^{-1}$  while  $n_e$  is the thermal electron density. The rotation measure (RM) is then defined as

$$\text{RM} \equiv \frac{d\theta(\lambda)}{d\lambda^2}, \quad (3)$$

and is equivalent to the FD in the case of a single source along the LOS without any internal Faraday rotation and beam depolarisation.

Throughout this paper we only consider LOSs parallel to the three common axes of the simulations with observers far in the positive direction such that every LOS along that axis stays parallel to other LOSs along the same axis. Furthermore, in this section the sources are taken far in the negative direction.

As the thermal electron density was not explicitly computed in the simulations, we model it using the following two different prescriptions similar to [Rappaz et al. \(2022\)](#).

- Mod1: the thermal electron density is proportional to the density

of the ISM  $n_e = c_n n$  with  $c_n$ <sup>1</sup> taken such that the mean thermal electron density is  $0.1 \text{ cm}^{-3}$  at each time step.

- Mod2: the thermal electron density is taken as constant and set to  $n_e = 0.1 \text{ cm}^{-3}$ .

Using Eq. (2), we then compute and compare the RM maps obtained with the two aforementioned models of thermal electron densities. In Fig. 3 we plot the contours of RM along the  $z$  axis for Mod1 and Mod2 of  $n_e$ . With Mod2 the typical values of RM are almost an order of magnitude smaller than that from Mod1, while the root mean squared (RMS) of the RM with Mod1 is about  $76 \text{ rad m}^{-2}$  compared to  $20 \text{ rad m}^{-2}$  with Mod2. With both models of  $n_e$  the mean RM is close to zero. Qualitatively, the observed structures in RM maps are larger with the second model as it is sensitive only to the magnetic field variations. Thus, we expect that the variations of RM in the plane of observation would be important on a larger scale if Mod2 represented the distribution of  $n_e$  correctly. We expect the occurrence of finer structures in the RM maps for more complex models of  $n_e$ , depending upon the cross correlations between magnetic fields and  $n_e$ , and their individual distributions as well. As such, for Mod1, in which  $n_e$  scales directly with the mass density of hydrogen, we do in fact see more small-scale structures (upper panel of Fig. 3). In principle, the scaling between the local distribution of thermal electrons and density could also depend on the local phase of the ISM.

A qualitative assessment of the shapes of these structures in RM maps suggests that they are anisotropic, in a sense that their correlation lengths are larger in one direction. This is presumably due to anisotropy in the magnetic field introduced by the background shear in the simulations. To analyse this assertion more systematically and to quantify the anisotropy, we compute the correlation lengths  $\ell$  from two point correlation functions of RM maps, which we define for an arbitrary function  $f(\mathbf{r})$  as

$$C_f(\mathbf{R}) = \langle f(\mathbf{r})f(\mathbf{r}') \rangle = \mathcal{F}^{-1}(|\mathcal{F}(f)|^2), \quad (4)$$

where  $\mathbf{R} = \mathbf{r} - \mathbf{r}'$  and  $\mathcal{F}$  is the usual Fourier transform. This results in elliptical structures centred at  $\mathbf{r} = \mathbf{r}'$  (see e.g. Fig. A1), which we normalise and integrate along any particular line starting from the centre to obtain the correlation length in that direction. We thus obtain the distribution of correlation lengths as a function of angle with respect to the radial direction. We summarise in Table 1 the orientation of these ellipses, that is the angle between the major-axis of the two point correlation contour with  $x$  axis in degrees. We have computed these angles during the kinematic and dynamical phases of the evolution separately, along with their  $1 - \sigma$  variances. It does not seem that model of  $n_e$  distribution has any significant impact on these orientations in the dynamical phase, and it appears that it is entirely decided by the background shear. The angle along which the maximum of the correlation lengths is situated, matches roughly with the one obtained for background shear in [Bendre & Subramanian \(2022\)](#). Nevertheless, with increasing SN rate the direction of the ellipses show larger variations of the mean value. We note however that estimates of variances in Run50 and Run100 could suffer from a lack of data points, the sampling being almost half of the one of Run25, and that Run25 is more sampled at the very beginning of the dynamical phase. We also show the time evolution of the ratio  $\ell_{\min}/\ell_{\max}$  (where  $\ell_{\min}$  and  $\ell_{\max}$  correspond roughly to the minor and major axis respectively of the two point correlations of RM maps) in

<sup>1</sup> Note that  $c_n$  is constant as long as the mean density of the simulation is preserved. At late times of our simulations a small amount of matter can be lost and thus  $c_n$  is adjusted accordingly.

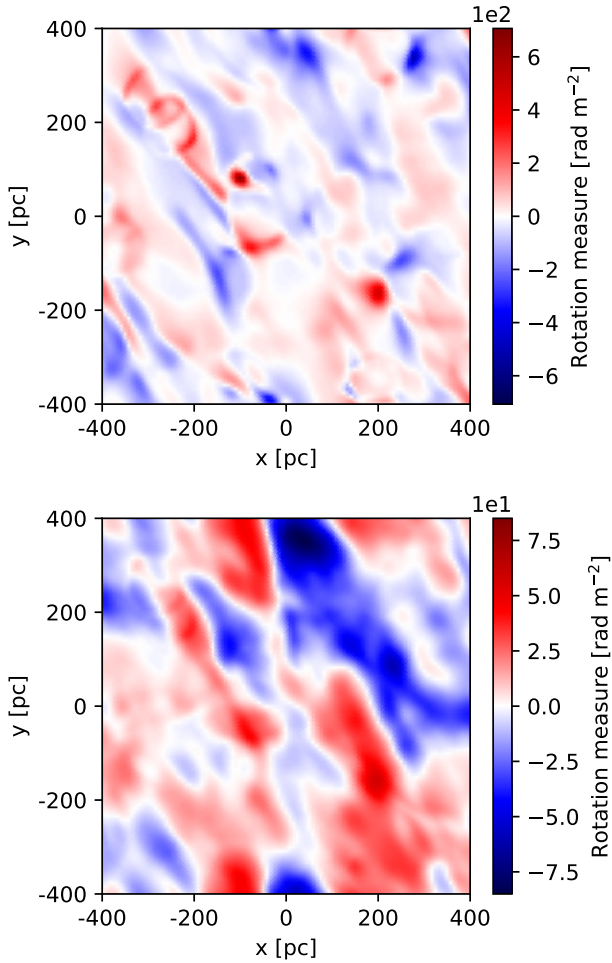


**Figure 3.** Rotation measure along the  $z$  axis for Run25 at  $T \approx 1508$  Myr. This time step is in the middle of the dynamical phase. *Top panel:* Mod1 is used, the thermal electron density is proportional to the ISM density. *Bottom panel:* Mod2 is used, the thermal electron density is constant across the box.

Fig. 4 and list its averages over the dynamical phase in Table 2 (see also Fig. A2).

We also study the correlation length of the RM maps in the plane of observation in more detail. In particular the ratio  $\ell_{\min}/\ell_{\max}$  shows an interesting behaviour. We clearly see in Fig. 4 that for both  $n_e$  models in the early stage of the simulations  $\ell_{\max}$  and  $\ell_{\min}$  are comparable. This is mainly due to the initial magnetic field that is uniform along the  $z$  axis. As the system evolves, the points farther away from each other no longer stay correlated and both  $\ell_{\max}$  and  $\ell_{\min}$  are reduced. However  $\ell_{\min}$  decreases faster than  $\ell_{\max}$  in the kinematic phase, indicating that the ellipses are stretched more and more with time due to differential rotation. Once the dynamical phase is reached the ratio is approximately constant; mean values of  $\ell_{\min}/\ell_{\max}$  can be found in Table 2. These average values grow non-linearly with the SN rate with a scaling slightly steeper for Mod2 than for Mod1. Furthermore, these ratios depend on the model of  $n_e$  as well, specifically the mean values of  $\ell_{\max}$  are systematically larger for the constant  $n_e$  model (Mod2), compared to Mod1. This is probably owing to the fact that there is an approximate correlation between magnetic fields and the mass density ( $B \sim \rho^{0.5}$ ), which makes the integrant of

		Run25	Run50	Run100
Kinematic	Mod1	$172 \pm 20$	$118 \pm 26$	$121 \pm 38$
	Mod2	$120 \pm 23$	$120 \pm 32$	$115 \pm 43$
Dynamical	Mod1	$119 \pm 10$	$125 \pm 13$	$126 \pm 30$
	Mod2	$120 \pm 14$	$123 \pm 18$	$125 \pm 30$

**Table 1.** Comparison for  $\text{RM}_z$  of the time average of the orientation of the maximum correlation length in degree for the two models of the free electron density and the three simulation data sets. The errors are taken as one standard deviation of the distribution.

Eq. (2) proportional to  $\sim \rho^{1.5}$  in Mod1, while it scales only as  $\sim \rho^{0.5}$  for Mod2 (as  $n_e$  is constant). Regarding the mean values of  $\ell_{\max}$  and  $\ell_{\min}$  in the dynamical phase (see Table 2), an increase of the SN rate reduces the elongation of the RM ellipses. The maximum correlation length is particularly affected by the choice of  $n_e$ . We note that  $\ell_{\max}$  compares well with the maximum correlation length of the anisotropic magnetic field reported in Bendre & Subramanian (2022). This two-point correlations function, at far away points from its origin predicts the anti-correlations (note the negative blue regions in Fig. A1, outside of the central red ellipse, along the  $\ell_{\min}$ ), and at some time steps these anti-correlations overwhelmingly contribute to the integration along  $\ell_{\min}$ , making the correlation length negative. Another relevant measure for the correlation length in such a case is similar to Taylor microscale, which counts the second order moments of the correlation function. It can be obtained by fitting a parabola to the curves in Fig. 4 and noting where the fit crosses the  $y = 0$  line.

Throughout our analysis of the RM maps we also noticed that the  $z$  axis is very peculiar. In fact, it is the only axis for which the RM maps distributions are more or less Gaussian and their standard deviations increase with time and are also systematically higher in Mod1 than that in Mod2. The  $z$  axis is not directly affected by differential rotation so the random fluctuations of the magnetic field and the thermal electron density along the LOS play a central role in determining the global structure of the map. More importantly these structures are formed on smaller scales than the ones induced by the mean magnetic field and electron density.

The RM maps along the  $x$  and  $y$  axes also display elliptical structures elongated along the, respectively,  $x$  and  $y$  axis (see Figs. B1 and B2). Typical structures are usually on length scales that are comparable to the entire domain for the  $y$  axis but not for the  $x$  axis (see Table B1 and Table B2). These maps are particularly peaked in the galactic plane where the magnetic field and density reach their maximum. As for the RM along the  $z$  axis, we also observe some bubble structures that could be due to the propagation of matter from SN explosions (shock fronts characterised by over dense regions). The evolution of the maximal correlation length is highly affected by the sign flipping of the  $x$  and  $y$  components of the magnetic field.

### 3.2 Synchrotron radiation

Relativistic charged particles emit synchrotron radiation when being accelerated. In the magnetised ISM, they are subject to the Lorentz force, so the acceleration is related to the mass and the velocity of the particle, as well as to the local magnetic field. Most of the synchrotron emission is caused by CR electrons, as they are relatively abundant, fast, and light. In this analysis we only consider these CR electrons as a source of the synchrotron radiation from our simulation box. In the most general case, an emitted photon is elliptically polarised in the plane of observation and for a group of highly relativistic electrons it can be shown (see e.g. Westfold 1959) that their total resulting



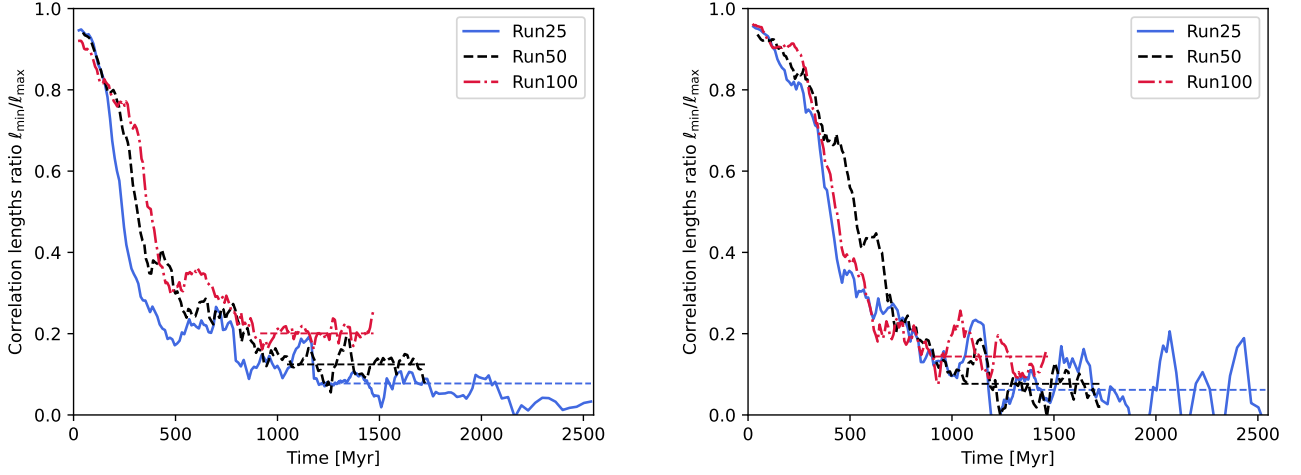


**Figure 4.** Evolution of the ratio of typical correlation lengths of the rotation measure along the  $z$  axis. Each data point is averaged over all data points within 50 Myr around its corresponding time. The thin horizontal lines indicate the average value over the dynamical phase. *Left panel:* Mod1 is used to compute the RM. *Right panel:* Mod2 is used to compute the RM.

		Run25	Run50	Run100
$\ell_{\min}/\ell_{\max}$	Mod1	$0.077 \pm 0.020$	$0.124 \pm 0.027$	$0.200 \pm 0.018$
	Mod2	$0.062 \pm 0.42$	$0.077 \pm 0.045$	$0.144 \pm 0.044$
$\ell_{\min}$ [pc]	Mod1	$6.8 \pm 1.7$	$10.2 \pm 2.3$	$14.8 \pm 1.5$
	Mod2	$6.7 \pm 5.8$	$8.2 \pm 5.1$	$15.9 \pm 5.4$
$\ell_{\max}$ [pc]	Mod1	$97 \pm 8$	$92 \pm 10$	$80 \pm 3$
	Mod2	$152 \pm 14$	$145 \pm 14$	$131 \pm 10$

**Table 2.** Comparison for  $RM_z$  of the time average in the dynamical phase of the correlation lengths ratio ( $\ell_{\min}/\ell_{\max}$ ), the minimum correlation length ( $\ell_{\min}$ ) and the maximum one ( $\ell_{\max}$ ) for the two models and the three simulation data sets. The errors are taken as one standard deviation of the distribution.

emission is linearly polarised in the plane of observation, with a plane of polarisation perpendicular to the projected magnetic field. The intrinsic polarisation angle of the synchrotron radiation is given by

$$\theta_i = \frac{\pi}{2} + \arctan \frac{B_2}{B_1}, \quad (5)$$

where the  $B_{1/2}$  denote the magnetic field components along two orthogonal axes perpendicular to the LOS.

As these photons pass through the ISM, they also undergo Faraday rotation; see Eq. (1). The polarisation angle of a cell of synchrotron radiation emission is given by

$$\theta = \theta_i + \lambda^2 FD'. \quad (6)$$

Note that the cell of emission suffers from its own Faraday rotation. Sokoloff et al. (1998) showed that in this case we need to subtract from the total FD one half of the FD of the emission cell, we call this quantity  $FD'$  to differentiate from Faraday rotation of a non emitting cell. Due to the ambiguity by a  $\pi$  rotation of the linearly polarised synchrotron emission angle, it is impossible to distinguish between coherent magnetic fields, with a constant direction along the LOS, and anisotropic magnetic fields, which reverse their sign.

We assume that the CR electron energy spectrum follows a power law of the form  $dN(E) \propto E^{-\gamma} dE$ . Under such assumptions, the intrinsic fractional polarisation (which does not include any depolar-

isation effect) can be expressed as (Longair 2011)

$$p_i = \frac{\alpha - 1}{\alpha - \frac{1}{3}}, \quad (7)$$

where  $\alpha = (1-\gamma)/2$  is the spectral index of the synchrotron radiation. In this paper we consider  $\gamma = 2.7$  (Kotera & Olinto 2011), which gives  $p_i \approx 0.74$ .

Following an approach similar to Sur et al. (2021) and Basu et al. (2019) we define the total synchrotron intensity map as

$$I_\nu = \int N_0 n_{\text{CR}} B_\perp^{1-\alpha} \nu^\alpha dl, \quad (8)$$

with the integration being performed along the LOS,  $n_{\text{CR}} = \int N(E) dE / \delta^3$ , which stands for the density of CR electrons,  $N_0$  is a proportionality constant in the CR power law while  $B_\perp$  is the component of magnetic field perpendicular to the LOS. Note that along the  $z$  axis we compute the RM through  $B_z$  which is expected to be dominated by random variations in our set-up. However, the synchrotron emission is obtained through  $B_x$  and  $B_y$  which capture the effects of the mean-field dynamo. As such, any quantity derived from this emission can also be used to characterise the effect of the mean-field over the system.

Since the simulations did not include CR, similarly to the density of thermal electrons, we prescribe the CR electron distribution also with two different models namely:

- CRMod1: Here, the CR electron density is proportional to the magnetic energy density. This model assumes that equipartition of CR and magnetic energy is achieved at all scales, and is preserved throughout the evolution.

- CRMod2: This model is based on a constant CR electron density. The assumption involved here is that the CR density variations are either too small or occur on the length scales that are too large to be relevant.

In order to generalise the discussion we normalise the synchrotron intensity map by its total flux and by this obtain a result that is independent on the frequency and on the CR normalisation  $N_0$ . The maps of synchrotron intensity show similar structures (see Fig. 5, Fig. B3 and Fig. B4) with both models, although CRMod1 tends to

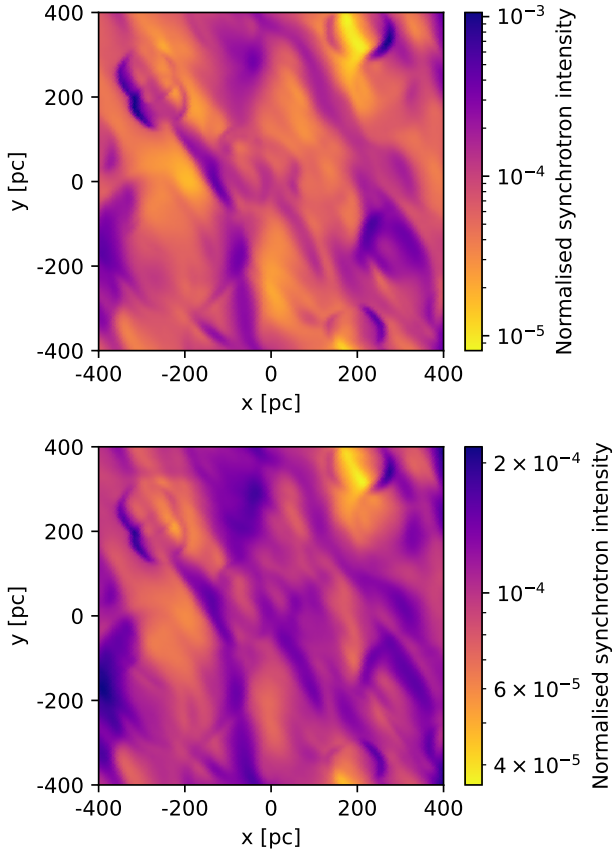


**Figure 5.** Normalised synchrotron radiation intensity along the  $z$  axis for Run25 at  $T \approx 1508$  Myr. This time is in the middle of the dynamical phase. *Top panel:* CRMod1 is used, which is based on equipartition between CR and magnetic energy. *Bottom panel:* CRMod2 is used, in which the CR electron density is constant across the box.

produce a larger range of values in synchrotron intensity. We illustrate this in Fig. 6 where we plot the probability distributions of total synchrotron intensity maps integrated along the  $z$  axis for both CR electron models, at various times. CRMod2 results in narrower distributions compared to CRMod1, which could also be ascribed to the cross-correlations between the density and the magnetic field inherent for CRMod1. The synchrotron intensity can be directly related to the magnetic field for both models this time. With the models used here  $I_\nu \propto \int (B_\perp^{3-\alpha} + B_\perp^{1-\alpha} B_\parallel^2) dl$  for CRMod1 and  $I_\nu \propto \int B_\perp^{1-\alpha} dl$  in the case of CRMod2. So the structures in the synchrotron map trace the magnetic field lines, that can be stretched due to the shearing and randomly twisted by the SN explosions. From the very similar qualitative aspects of the two maps with the two different models of CRs, we conclude that it is mainly the magnetic field strength that characterises the structures. In fact, most of the structures in the synchrotron intensity maps are also present in the mean magnetic field strength over  $x - y$  plane (see Fig. 2).

The  $z$  axis is also peculiar regarding the distributions of the synchrotron radiation (see Fig. 6) as a lognormal distribution of synchrotron intensity is observed only for this axis. It is clear from this plot that the distributions of  $I_\nu$  starts out with a peak at the lower values and with a flat tail, and tends eventually to an approximately symmetric shape. The mean value shifts with time as the magnetic

field energy is growing. Contrary to the RM, the synchrotron radiation associated with both models of CR electron distribution is not a linear function of the magnetic field. Therefore, any random fluctuations therein would not lead to a Gaussian but rather to a lognormal distribution.

We also note that when we take the telescope effects (Sec. 4) into account, we observe a reduction of the distribution tails, since this amounts to filtering over the small scale structures. The inclusion of telescope effects is also accompanied by a slight shift of the distributions to the lower normalised synchrotron intensities.

### 3.3 Stokes parameters

The Stokes parameters allow to characterise the polarisation state of a beam (e.g. Taylor et al. 2003; Haverkorn et al. 2006; Planck Collaboration et al. 2015; Clark & Hensley 2019). In this paper we consider synchrotron emission as the only source of the observed radio beam and its total intensity is given by  $I_\nu$ , as defined in Eq. (8). The  $Q$  parameter is the relative degree of linear polarisation along two arbitrary orthogonal axes and the  $U$  parameter is the relative degree of linear polarisation along the same two axes rotated by  $\pi/4$ . Here, we ignore the Stokes  $V$  parameter as we are only considering a linearly polarised signal. Since we are free to choose the orthogonal axes, we can conveniently define

$$Q_\nu = \int p_i N_{0\text{CR}} B_\perp^{1-\alpha} \nu^\alpha \cos(2\theta) dl, \quad (9)$$

$$U_\nu = \int p_i N_{0\text{CR}} B_\perp^{1-\alpha} \nu^\alpha \sin(2\theta) dl, \quad (10)$$

with  $\theta$  given in Eq. (6). The polarisation state of the complete beam is affected by Faraday effects, and the properties of its polarised component such as the intensity of the linearly polarised signal and the angle of polarisation are defined in terms of the Stokes parameters as (Gardner & Whiteoak 1966)

$$PI_\nu = \sqrt{Q_\nu^2 + U_\nu^2}, \quad \Gamma_\nu = \frac{1}{2} \arctan\left(\frac{U_\nu}{Q_\nu}\right). \quad (11)$$

We note that, in practice, there is an ambiguity in determining this angle since with the ratio  $U_\nu/Q_\nu$  we lose the information of the signs of  $U_\nu$  and  $Q_\nu$  separately. We thus use the function  $\arctan2$  and the modulus of  $\pi$  to compute the polarisation angle such that  $\Gamma_\nu \in [0, \pi]$ . The degree of linear polarisation (DOP) is then simply given by  $p_\nu = PI_\nu/I_\nu$  and is in general decreasing with wavelength due to Faraday effects (see Sokoloff et al. 1998).

In Fig. 7 we show the depolarisation which is the ratio of the observed DOP and the intrinsic polarisation of synchrotron radiation  $p_\nu/p_i$ . We observe that in the limits of large and small frequencies it reaches constant values that depend on the CR ray model. The depolarisation we calculate here results only from the differential rotation of the plane of polarisation induced by the Faraday effects and the addition of cells of emission along the LOS. When the observation frequency is very large the Faraday effects are very small and thus the depolarisation corresponds to the intrinsic state of the magnetic field along the LOS. The value should depend upon the distribution of synchrotron intensity and its intrinsic angle of polarisation along the LOS. In the very low frequency regime the Faraday effects are so large that any correlation between the different intrinsic angle of polarisation is lost, which leads to a large decrease in the DOP. Its value then tends to the one obtained with a completely random distribution of angles. In the intermediate regime however, the evolution of the mean depolarisation with the frequency is mainly dependent on the thermal electron distribution model. Since we have a certain

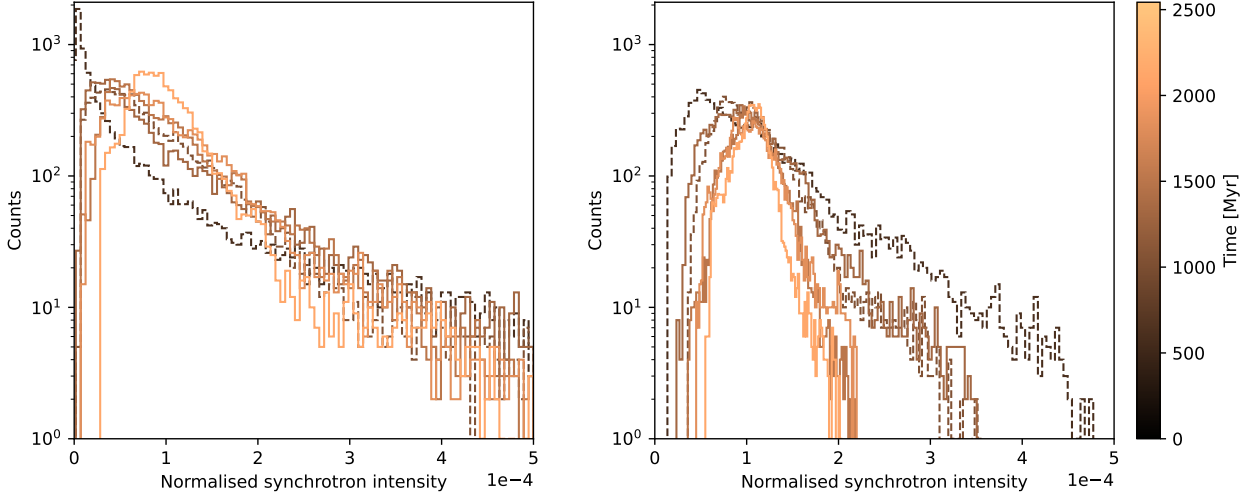


**Figure 6.** Distributions of the synchrotron radiation along the  $z$  axis for Run25 at the frequency  $\nu = 1.4$  GHz. Histograms shown with dashed lines are taken in the kinematic phase, whereas solid lines correspond to the dynamical phase of the dynamo. *Left panel:* CRMod1 is used, which is based on equipartition between CR and magnetic energy. *Right panel:* CRMod2 is used, in which the CR electrons density is constant across the box.

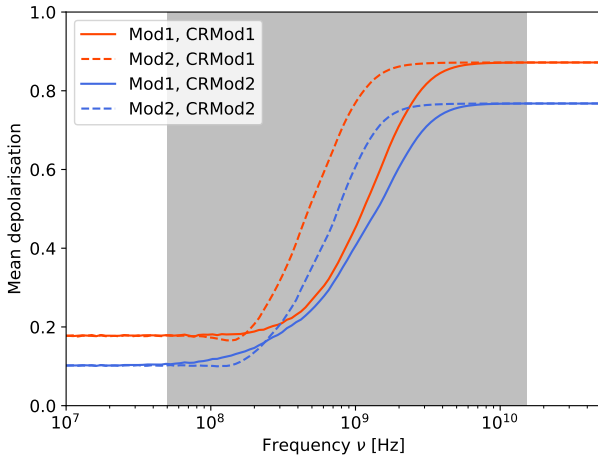


**Figure 7.** Dependence of the mean observed depolarisation ( $\langle p_\nu/p_i \rangle$ ) along the  $z$  axis on the frequency of observation for the four different configurations of previously defined models for Run25 at  $T \approx 1508$  Myr. The greyed out area represents the frequency range of observation of SKA (Dewdney et al. 2013).

distribution of FD along the LOS, the frequency at which the term  $FD\lambda^2$  becomes negligible is not the same for each cell of synchrotron emission. Especially, the frequency at which the mean depolarisation starts to increase, and thus the transit from one constant regime to the other (see Fig. 7), will give the order of magnitude of the lowest absolute values of FD encountered along the LOS in the plane where the average is performed. The same is also true for the upper bound of the transition but this time for the highest values of FD.

We find that the typical structures in the total synchrotron intensity maps are very similar to the ones observed for the polarised intensity for very high frequency. In the first row of Fig. 8 we show the observed polarised intensity along the  $z$  axis at, respectively, 70 MHz, 1.4 GHz and 5 GHz using the configuration of models that is perhaps more realistic (Mod1 and CRMod1). We observe throughout these

typical maps that the nature of observed structures depends strongly on the frequency of observation. Especially on low frequencies we completely lose the details on small spatial scales. We also note that our normalisation of the total incoming flux due to the synchrotron effects is arbitrarily fixed, so the typical values that we obtained should not be directly compared to real observations, which is why we normalise each map by its total flux. The spacial distribution of these structures, however, are unaffected by this normalisation.

The DOP and the observed polarisation angle are also affected by the frequency (row 2 and lines in row 1 of Fig. 8). Contrary to the polarised intensity maps (in row 1), the structures are no longer smoothed when the frequency is decreased but are mostly destroyed. In the very low frequency regime, the typical structures are of the order of a pixel, which we also confirm from the evolution of the correlation length as a function of the frequency of observation. There, a similar transition to the one presented in Fig. 7 is observed. Furthermore, the DOP maps in the intermediate frequency regime show new elongated structures that are oriented with respect to the radial ( $x$ ) axis, which could be due to the differential rotation.

In the high frequency regime the DOP is relatively uniform due mainly to the correlation of the orientation of the projected magnetic field along the LOS. In particular, at 5 GHz the observed angle of polarisation is almost always perpendicular to the orientation of the projected mean magnetic field (see Fig. 2) since the Faraday effects are small. However, when the frequency of observation is decreased this statement no longer holds and the correlation between the polarisation state and the magnetic field is lost. In Appendix Sec. B we also display the equivalent to Fig. 8 for the  $x$  and  $y$  axes (Fig. B5 and Fig. B6).

#### 4 TELESCOPE EFFECTS

In this section we describe the effects of a finite telescope resolution on the observables extracted from the simulations. In order to make a comparison with actual observations we smooth the observed maps with a Gaussian kernel (Thompson et al. 2017), with the aim of simulating the aforementioned effect of finite telescope resolution. We use

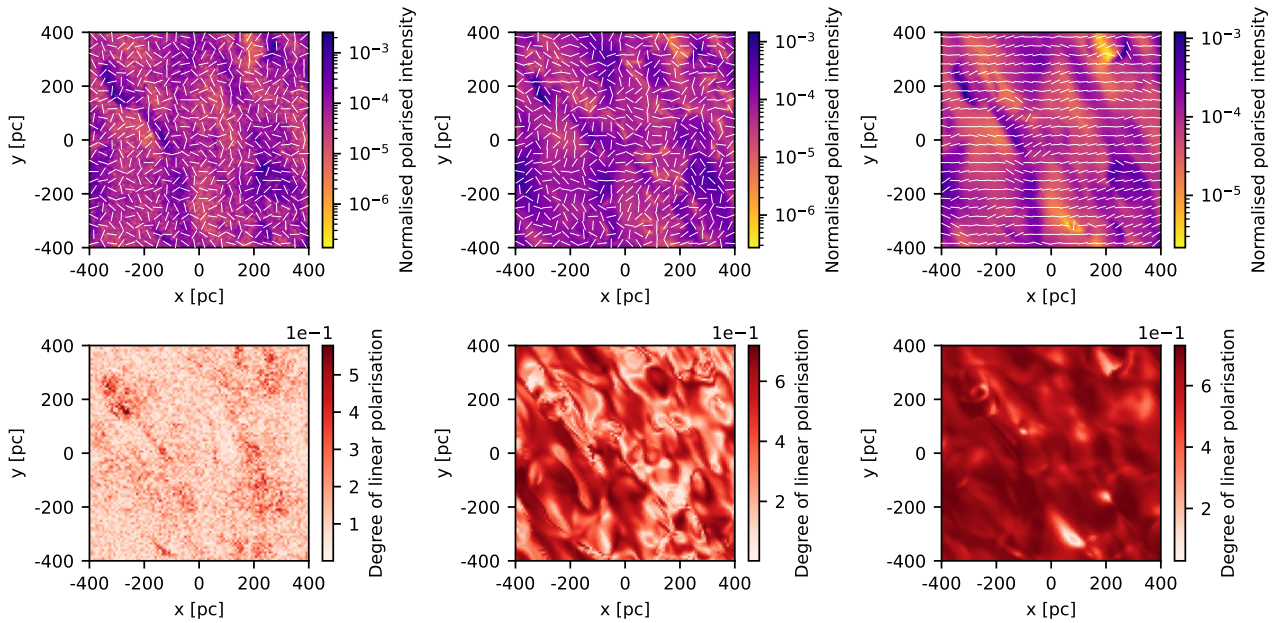


**Figure 8.** *First row:* Normalised polarised intensity maps  $PI_v$ , with respect to the  $z$  axis. The lines indicate the observed angle of polarisation  $\Gamma_v$ , with respect to the  $z$  axis. *Second row:* Degree of linear polarisation  $p_v$ , with respect to the  $z$  axis. The three columns correspond, respectively, to a frequency of observation of 70 MHz, 1.4 GHz, and 5 GHz for Run25 at  $T \simeq 1508$  Myr, i.e. in the dynamical phase. We used Mod1 and CRMod1 to compute all the presented quantities.

a convolution kernel with a full width at half-maximum (FWHM) being the same in all directions. It mainly leads to a deletion of the small scale structures while preserving the larger ones. However, we need to treat the DOP and polarisation angle maps more carefully as they are obtained through the transformation of the actual observables, i.e. the Stokes parameters  $Q$  and  $U$ . In practice, observations thus depend upon the frequency of observation as well as the resolution of the used telescope.

We set the FWHM of the Gaussian kernel to 5 pixels which corresponds to a smoothing scale of  $\sim 42$  pc. If we consider, for example, that the telescope can achieve a resolution of 0.5 arcsec, the resolution of  $\sim 42$  pc would locate the galaxy at  $\sim 17$  Mpc. When comparing the properties of RM maps with (Fig. 9) and without (Fig. 3) the telescope effects we see that we have lost the very small scale details like the bubbles structures in the upper left corner of Mod1. The RMS values are reduced to 57 and 18  $\text{rad m}^{-2}$  for Mod1 and Mod2, respectively. On the other hand, we recover qualitatively the overall information encoded in the large scale ellipses of the maps, like the sign of the mean magnetic field along the LOS or the orientation of the structures. Note however that the peaked areas of the RM map associated with Mod1 have been erased. The length scales are not affected significantly but are increased by  $\sim 5$  pc which is about 5% of its original value. We also note that a study of the RM at a significantly higher redshift would require a modification of the Eq. (2) (see e.g. Akahori & Ryu 2011).

In Fig. 10 we present the exact same maps as in Fig. 8 but corrected by telescope effects. We clearly see that the filaments and arc structures in the polarised intensity contours are still identifiable but thickened, thus the small scale details are not distinguishable from the background. There are also differences in the evolution regarding the frequency of observation. If we focus on the lowest values of the maps we see that they are spatially distributed in such a way that they delimit structures of higher values without agglomerating or forming large scale structures themselves. It is then even harder to disentangle between the original peaked structures and the new structures

induced by the Gaussian smoothing. The effect on the DOP and angle of polarisation are even more pronounced as we cannot achieve the same random pixel-wise maps on frequencies  $\nu \sim 70$  MHz. In particular, telescope effects lead to the creation of structures that we do not observe in maps with the maximum resolution of the simulation, i.e.  $\delta \sim 8$  pc. However, it seems that at very low frequencies the isotropy observed at the maximum resolution is still observed with telescope effects for these two quantities. Furthermore, we observe that the typical values of DOP and normalised polarised intensity are reduced by Gaussian smoothing.

The overall shapes of the curves in Fig. 7 are not affected by the telescope effects; indeed the constant value of the mean depolarisation in the high and low frequency limit still depends mainly on the CR distribution model, and the intermediate transition region still depends on the model of thermal electrons. However we still can notice differences. The mean depolarisation at low frequencies is significantly lower and closer to zero. The frequency range of transition is smaller, especially the end of the transition at low frequencies occurs at a higher frequency ( $\nu \sim 0.5$  GHz compared to  $\nu \sim 0.1$  GHz without telescope effects). This trend is also confirmed in Fig. 11, where we show the evolution of the mean depolarisation as we increase the FWHM of the Gaussian kernel and the frequency of observation. This evolution is not linear and highly depends on the frequency of observation. The telescope effects are particularly important at low and intermediate observation frequencies, as we could directly see from the DOP maps (see second row of Fig. 10). It also supports the idea that when we have a finite resolution observation we lose more the information generated by the lowest values of FD along the LOS. This is different from the RM maps where we lost most of the information on the structures generated by the highest values of RM.



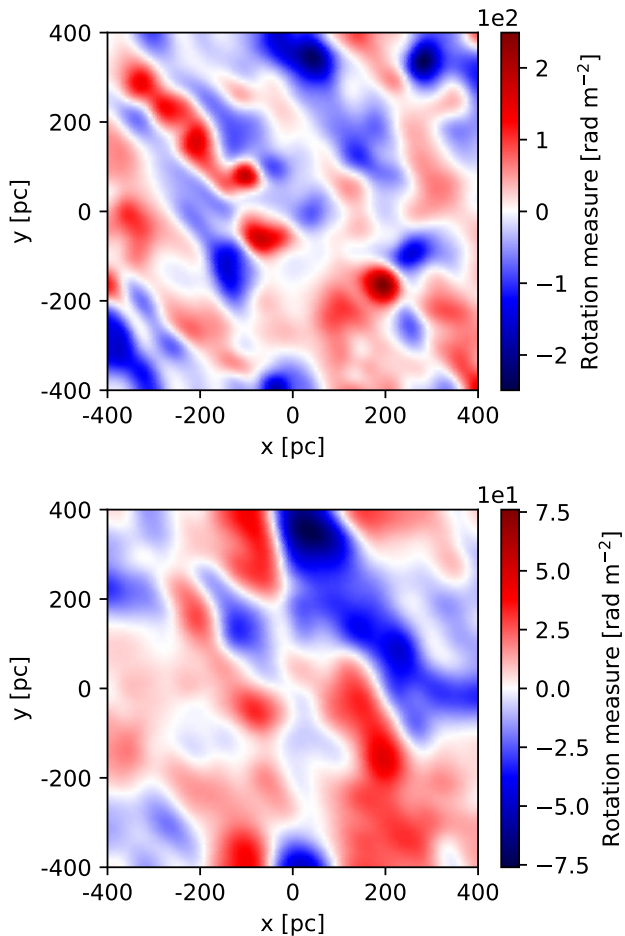


**Figure 9.** Rotation measure along the  $z$  axis for Run25 at  $T \approx 1508$  Myr. This time step is in the middle of the dynamical phase. The two maps are smoothed by a Gaussian kernel of  $5 \times 5$  pixels. *Top panel:* Mod1 is used, the thermal electron density is proportional to the ISM density. *Bottom panel:* Mod2 is used, the thermal electron density is constant across the box.

## 5 DISCUSSION

In this section we discuss the main limitations of this work. First, we would like to point out that the simulations domain is much smaller than a typical disc galaxy in  $x$  and  $y$  directions. For example the Milky Way has a radial length scales of  $\sim 30$  kpc, as opposed to  $\sim 0.8 \times 0.8$  kpc spanned by the simulation domain in  $x$  and  $y$  direction. Any extracted observable thus would therefore reveal the local correlations in the ISM turbulence, and any correlations exceeding a kpc scale would not be captured. Furthermore, the reconstruction of RM maps of an entire galaxy would also need the radial dependence of gas distribution and any azimuthal asymmetries to be taken into account (Bosma 1981). That is the main reason we performed our analysis along the  $z$  direction.

We already mentioned that the simulations analysed only include neutral hydrogen but in reality several species could have non negligible contribution to the ISM dynamic. Especially this treatment does not allow us to get a self consistent evaluation of the thermal and CR electrons densities. We had to define very simple models for both of them. The mean free electron density used here is set to  $0.1 \text{ cm}^{-3}$ , especially with Mod2 we neglect any kind of spatial and temporal variations. From observations we know that in spiral galax-

ies the mean thermal electron density can range between  $\sim 0.1$ - $0.01 \text{ cm}^{-3}$  in the disc plane depending if we consider arms or inter-arm regions (Schnitzeler 2012; Yao et al. 2017; Beck et al. 2019). However, the free electron density is expected to be even smaller outside the disc plane. As the scale height of the simulation box is larger than a typical disc, the mean free electron could be overestimated. With Mod1 we neglect contributions from other parameters, such as temperature, to evaluate the local thermal electron density.

Even stronger assumptions were made regarding the CR models. A constant CR model would hold only on very small scales and not at all on a galactic scale. On the contrary, equipartition seems not to hold on scales smaller than  $\sim 1$  kpc (Stepanov et al. 2013; Yoast-Hull et al. 2016), whereas in this work our maximum resolution for any quantity is about 8.3 pc. We would need a more rigorous model that lies in between our two hypotheses. As an example a more complete description is proposed by Schober et al. (2016) that includes contributions to the CR spectrum from the main interactions of electrons in galaxies. However, this model does not include the diffusion of cosmic rays (see e.g. Sampson et al. 2022, for an analysis of the CR diffusion). Treating the CRs directly in the simulations can also affect the magnetic field itself (Bendre et al. 2020) which eventually affects all the observables presented.

We also would like to review effects that can modify the slope of the synchrotron emission spectrum, we used a constant value of  $\alpha = -0.85$  which would correspond to a typical value in the GHz frequencies (Platania et al. 1998). In practice when going to frequencies  $\nu \ll \text{GHz}$  the spectrum is modified due to the contributions from synchrotron self-absorption and free-free absorption. In the opposite when going higher than a few GHz we should include effects of free-free emission, eventually at very high frequency thermal emission could also be considered. These different interactions contribute together to flatten the synchrotron spectrum (Guzmán et al. 2011; Kogut 2012). It could be a straight forward extension of this work to see how the observables and observed structures are affected by these effects at large and low frequencies.

## 6 CONCLUSIONS

In this paper we have explored the typical observational signatures of a galactic magnetic field that has been self-consistently generated by a large-scale turbulent dynamo. In particular we looked at three types of observables namely the Faraday RM, the synchrotron radiation, and the Stokes parameters, as well as their related quantities such as the DOP (Sec. 3). In the second part we applied simple telescope effects (Sec. 4) to mimic radio observations.

The magnetic field was directly obtained from a simulation of a galactic dynamo, while other relevant quantities for galactic radio emission were not included in the simulation. In particular, we had to model the distribution of thermal and non-thermal electrons. We have defined two models of thermal electrons, one with a constant electron density while in the other one we let the electron density scale with the local mass density. Similarly for CR electrons density, we used a model with constant CR density and in the other one we scaled it with magnetic energy density.

We found that the RM structures are consistent with the direction of differential rotation in the  $x - y$  plane. The SN rate does not seem to have an influence on the overall orientation of the structures in the dynamical phase. However it was noticed that the stability and the typical sizes of these structures are affected by the SN rate.

Our results also indicate that the RM is sensitive to the choice of the thermal electron model both in terms of qualitative aspect of the

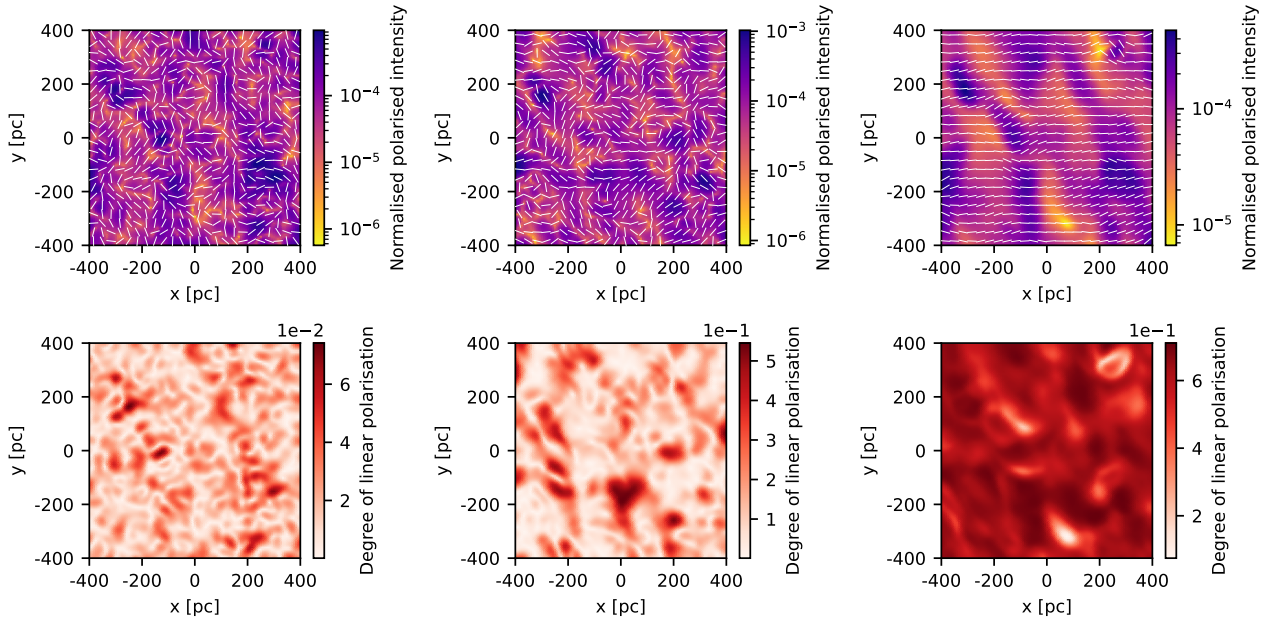


**Figure 10.** *First row:* Normalised polarised intensity maps  $PI_\nu$  with respect to the  $z$  axis. The lines indicate the observed angle of polarisation  $\Gamma_\nu$  with respect to the  $z$  axis. *Second row:* Degree of linear polarisation  $p_\nu$  with respect to the  $z$  axis. The three columns correspond, respectively, to a frequency of observation of 70 MHz, 1.4 GHz, and 5 GHz for Run25 at  $T \approx 1508$  Myr, i.e. in the dynamical phase. We used Mod1 and CRMod1 to compute all the presented quantities. All six maps are obtained after smoothing the observable with a Gaussian kernel with FWHM of 5 pixels.

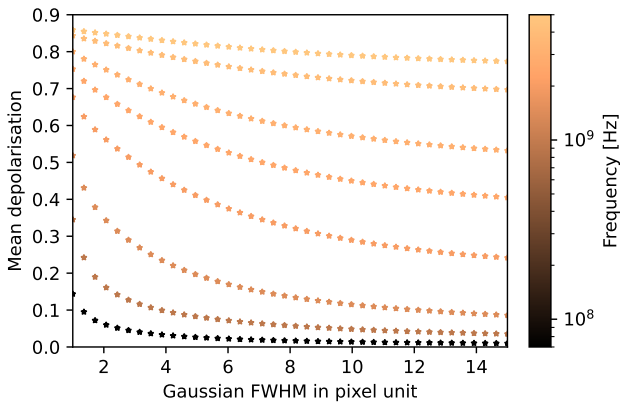


**Figure 11.** Evolution of the mean depolarisation  $\langle p_\nu/p_i \rangle$  along the  $z$  axis for Run25 at  $T \approx 1508$  Myr as a function of the Gaussian kernel used to simulate telescope effects. The depolarisation is computed using Mod1 and CRMod1.

structures and typical values of the maps. From the RM distribution we found that along an axis not directly influenced by rotation measure (i.e. the  $z$  axis in our setup) it is the magnetic field and thermal electron density variations that dominate the resulting maps.

Synchrotron radiation intensity maps showed the same structures as in the mean magnetic field maps. We found that the final qualitative aspect of the maps almost does not depend on the choice of the model of CR electron. However distributions showed a significantly increased degree of symmetry with the constant CR model along the  $z$  axis. Maps of quantities that are derived from the Stokes parameters maps are highly dependent on the frequency of observation. We found that decreasing the frequency introduces something similar to

a background noise over the maps, deleting structures. It was also observed that at an intermediate frequency completely new structures could appear, this frequency depends on the typical FD encountered in the photon's path.

Under telescope effects at a resolution of FWHM  $\sim 42$  pc, we observed mainly deletion of small scale spatial structures in every map. We also found that these effects depend non-linearly on the frequency of observation. In particular when we applied telescope effects, completely new structures in the contours of various quantities related to the Stokes parameters were observed at low frequencies. In the low frequency regime, the typical structures are mainly induced by FD values for which the term  $\lambda^2 FD'$  (with  $FD'$  being the FD for a self-emitting cell) is neither too large nor negligible. When this term is very large the cell of emission loses its correlation with the other cells along the LOS, thus a tiny variation in the frequency of observation will result in a random modification of Stokes  $Q$  and  $U$ . On the other hand when it is small, the cell of emission will not modify Stokes  $Q$  and  $U$ . Finally, if  $FD$  is such that  $\lambda^2 FD'$  is somewhere in-between, modifications in Stokes  $Q$  and  $U$  due to a frequency variation are smooth. As such the telescope effects seem stronger at the lower frequencies, the Gaussian smoothing tends to alter the information given by lowest values of FD more than high values. However we observed in RM maps that the deletion of small scale details happened primarily on the highest values of RM.

With this work we would like to motivate observational analyses that study the RM and Stokes parameters simultaneously, as they give complementary information about the magnetic field. We would like to emphasise that at low frequencies observations might suffer from the effect of a finite resolution and may therefore lead to wrong conclusions. With the new generation of telescopes, such as the Square Kilometre Array (SKA), however, the resolution of radio observations will highly increase which might allow lower frequencies to be explored increasing the comprehension of galactic magnetic fields.

## ACKNOWLEDGEMENTS

We are grateful to Kandaswamy Subramanian and Yoan Rappaz for providing very useful comments on our manuscript. A.B. and J.S. acknowledge the support by the Swiss National Science Foundation under Grant No. 185863.

## DATA AVAILABILITY

Data used in this analysis scripts will be provided upon reasonable request to the corresponding author

## REFERENCES

- Akahori T., Ryu D., 2011, *ApJ*, **738**, 134
- Basu A., Fletcher A., Mao S. A., Burkhart B., Beck R., Schnitzeler D., 2019, *Galaxies*, **7**, 89
- Beck R., 2004, *Astrophysics and Space Science*, **289**, 293
- Beck R., Wielebinski R., 2013, *Magnetic Fields in Galaxies*. Springer Netherlands, Dordrecht, pp 641–723, doi:10.1007/978-94-007-5612-0\_13, https://doi.org/10.1007/978-94-007-5612-0\_13
- Beck R., Chamandy L., Elson E., Blackman E. G., 2019, *Galaxies*, **8**, 4
- Bendre A. B., Subramanian K., 2022, *MNRAS*, **511**, 4454
- Bendre A., Gressel O., Elstner D., 2015, *Astronomische Nachrichten*, **336**, 991
- Bendre A. B., Elstner D., Gressel O., 2020, *Monthly Notices of the Royal Astronomical Society*, **500**, 3527
- Bernet M. L., Miniati F., Lilly S. J., Kronberg P. P., Dessauges-Zavadsky M., 2008, *Nature*, **454**, 302–304
- Bhat P., Subramanian K., 2013, *Monthly Notices of the Royal Astronomical Society*, **429**, 2469
- Biermann L., 1950, *Zeitschrift Naturforschung Teil A*, **5**, 65
- Bosma A., 1981, *The Astronomical Journal*, **86**, 1825
- Brandenburg A., Subramanian K., 2005, *Physics Reports*, **417**, 1–209
- Burn B., 1966, *Monthly Notices of the Royal Astronomical Society*, **133**, 67
- Clark S., Hensley B. S., 2019, *The Astrophysical Journal*, **887**, 136
- Dewdney P., Turner W., Millenaar R., McCool R., Lazio J., Cornwell T., 2013, Document number SKA-TEL-SKO-DD-001 Revision, 1
- Ferrière K. M., 2001, *Rev. Mod. Phys.*, **73**, 1031
- Fletcher A., 2010, in *Kothes R., Landecker T. L., Willis A. G., eds, Astronomical Society of the Pacific Conference Series Vol. 438, The Dynamic Interstellar Medium: A Celebration of the Canadian Galactic Plane Survey*. p. 197 (arXiv:1104.2427)
- Gardner F., Whiteoak J., 1966, *Annual Review of Astronomy and Astrophysics*, **4**, 245
- Gent F., Shukurov A., Sarson G., Fletcher A., Mantere M., 2013, *Monthly Notices of the Royal Astronomical Society: Letters*, **430**, L40
- Gressel O., Elstner D., Ziegler U., Rüdiger G., 2008, *Astronomy & Astrophysics*, **486**, L35
- Guzmán A. E., May J., Alvarez H., Maeda K., 2011, *A&A*, **525**, A138
- Hanasz M., Wółtański D., Kowalik K., 2009, *The Astrophysical Journal*, **706**, L155
- Haverkorn M., Gaensler B., McClure-Griffiths N., Dickey J., Green A., 2006, *The Astrophysical Journal Supplement Series*, **167**, 230
- Kandus A., Kunze K. E., Tsagas C. G., 2011, *Phys. Rep.*, **505**, 1
- Kogut A., 2012, *The Astrophysical Journal*, **753**, 110
- Kotera K., Olinto A. V., 2011, *Annual Review of Astronomy and Astrophysics*, **49**, 119–153
- Krause M., 2008, arXiv preprint arXiv:0806.2060
- Krause F., Raedler K. H., 1980, *Mean-field magnetohydrodynamics and dynamo theory*. Pergamon
- Krumholz M. R., Federrath C., 2019, *Frontiers in Astronomy and Space Sciences*, **6**, 7
- Kulsrud R. M., Cen R., Ostriker J. P., Ryu D., 1997, *ApJ*, **480**, 481
- Longair M. S., 2011, *High Energy Astrophysics*, 3 edn. Cambridge University Press, doi:10.1017/CBO9780511778346
- Parker E. N., 1971, *ApJ*, **163**, 255
- Planck Collaboration et al., 2015, *A&A*, **576**, A104
- Platania P., Bensadoun M., Bersanelli M., Amici G. D., Kogut A., Levin S., Maino D., Smoot G. F., 1998, *The Astrophysical Journal*, **505**, 473
- Price D. J., Bate M. R., Dobbs C. L., 2009, *Magnetic fields in star formation: from galaxies to stars* (arXiv:0804.4647)
- Rädler K. H., 1969, *Monats. Dt. Akad. Wiss.*, **11**, 194
- Rappaz Y., Schober J., Girichidis P., 2022, *MNRAS*, **512**, 1450
- Sampson M. L., Beattie J. R., Krumholz M. R., Crocker R. M., Federrath C., Seta A., 2022, *Monthly Notices of the Royal Astronomical Society*
- Sánchez-Salcedo F. J., Vázquez-Semadeni E., Gazol A., 2002, *ApJ*, **577**, 768
- Schnitzeler D. H. F. M., 2012, *Monthly Notices of the Royal Astronomical Society*, **427**, 664
- Schober J., Schleicher D. R. G., Klessen R. S., 2013, *A&A*, **560**, A87
- Schober J., Schleicher D. R. G., Klessen R. S., 2016, *ApJ*, **827**, 109
- Shakura N. I., Sunyaev R. A., 1973, *A&A*, **24**, 337
- Shukurov A., Sokoloff D., Subramanian K., Brandenburg A., 2006, *Astronomy & Astrophysics*, **448**, L33
- Sofue Y., Fujimoto M., Wielebinski R., 1986, *Annual review of astronomy and astrophysics*, **24**, 459
- Sokoloff D. D., Bykov A. A., Shukurov A., Berkhuijsen E. M., Beck R., Poezd A. D., 1998, *MNRAS*, **299**, 189
- Stepanov R., Shukurov A., Fletcher A., Beck R., La Porta L., Tabatabaei F., 2013, *Monthly Notices of the Royal Astronomical Society*, **437**, 2201
- Subramanian K., 2016, *Reports on Progress in Physics*, **79**, 076901
- Subramanian K., Narasimha D., Chitre S., 1994, *Monthly Notices of the Royal Astronomical Society*, **271**, L15
- Sur S., Bhat P., Subramanian K., 2018, *MNRAS*, **475**, L72
- Sur S., Basu A., Subramanian K., 2021, *MNRAS*, **501**, 3332
- Taylor A., et al., 2003, *The Astronomical Journal*, **125**, 3145
- Thompson T. A., Quataert E., Waxman E., Murray N., Martin C. L., 2006, *The Astrophysical Journal*, **645**, 186
- Thompson A. R., Moran J. M., Swenson George W. J., 2017, *Interferometry and Synthesis in Radio Astronomy*, 3rd Edition. Springer, Cham, doi:10.1007/978-3-319-44431-4
- Westfold K. C., 1959, *ApJ*, **130**, 241
- Yan H., Lazarian A., 2008, *The Astrophysical Journal*, **673**, 942
- Yao J. M., Manchester R. N., Wang N., 2017, *ApJ*, **835**, 29
- Yoast-Hull T. M., Gallagher J. S., Zweibel E. G., 2016, *MNRAS*, **457**, L29
- Zeldovich Y. B., Ruzmaikin A. A., Sokoloff D. D., 1990, *The almighty chance*. WORLD SCIENTIFIC, doi:10.1142/0862
- Ziegler U., 2004, *Computer Physics Communications*, **157**, 207

## APPENDIX A: TWO-POINT CORRELATION OF THE RM

In this section we illustrate the way we compute the correlation length. Fig. A1 represents an example of two-point correlation maps for the RM along the  $z$  axis. Fig. A2 shows the correlation function along the axes of maximum and minimum correlation length, which are simply obtained by integration.

## APPENDIX B: OBSERVABLES ALONG RADIAL AND AZIMUTHAL DIRECTIONS

We display in this section the results obtained for other two axes of the simulation, namely the radial  $x$  and azimuthal  $y$  directions. Typical correlation lengths of the RM in the dynamical can be found in Table B1 for the  $x$  axis and in Table B2 for the  $y$  axis. The equivalent maps to Fig. 3 for the other two axes are shown in Fig. B1 and Fig. B2. The normalised synchrotron intensity along, respectively, the  $x$  and  $y$  directions can be found in Fig. B3 and Fig. B4. Finally in Fig. B5 and Fig. B6 the six contour plots of Fig. 8 can be found for a LOS along the radial and azimuthal directions.

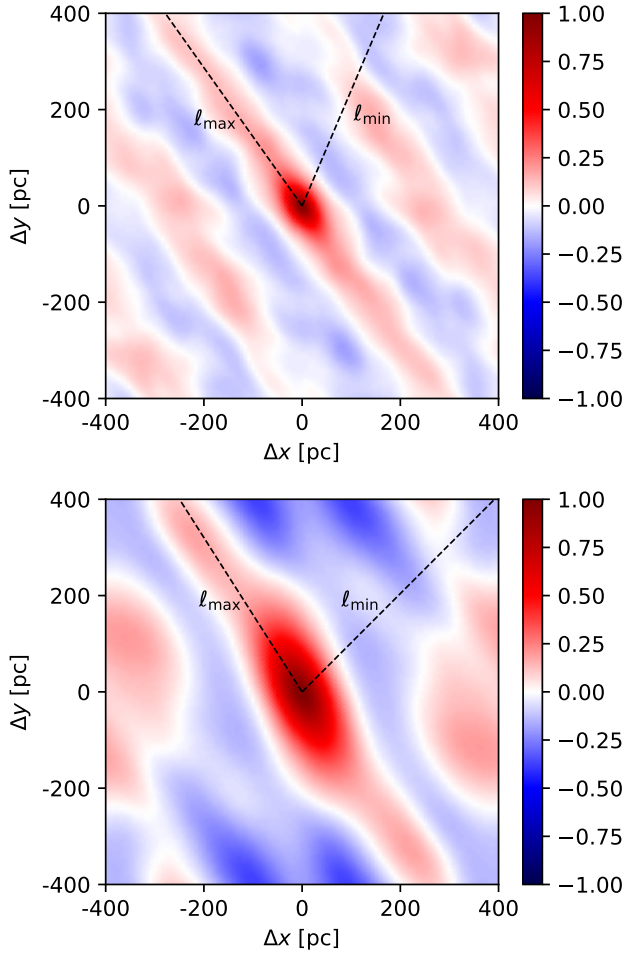


**Figure A1.** Rotation measure correlation function  $C_{RM}$  along the  $z$  axis for Run25 at  $T \approx 1508$  Myr. This time step is in the middle of the dynamical phase. *Top panel:* Mod1 is used, the thermal electron density is proportional to the ISM density. *Bottom panel:* Mod2 is used, the thermal electron density is constant across the box.

		Run25	Run50	Run100
$\ell_{\min}$ [pc]	Mod1	$54 \pm 8$	$45 \pm 4$	$60 \pm 3$
	Mod2	$44 \pm 7$	$40 \pm 5$	$68 \pm 4$
$\ell_{\max}$ [pc]	Mod1	$116 \pm 11$	$96 \pm 5$	$92 \pm 6$
	Mod2	$124 \pm 10$	$104 \pm 4$	$103 \pm 5$

**Table B1.** Comparison for  $RM_x$  of the time average over the last 500 Myr of each run of the minimum correlation length ( $\ell_{\min}$ ) and the maximum one ( $\ell_{\max}$ ) for the two models and the three simulation data sets. The errors are taken as one standard deviation of the distribution.

This paper has been typeset from a  $\text{\TeX}/\text{\LaTeX}$  file prepared by the author.

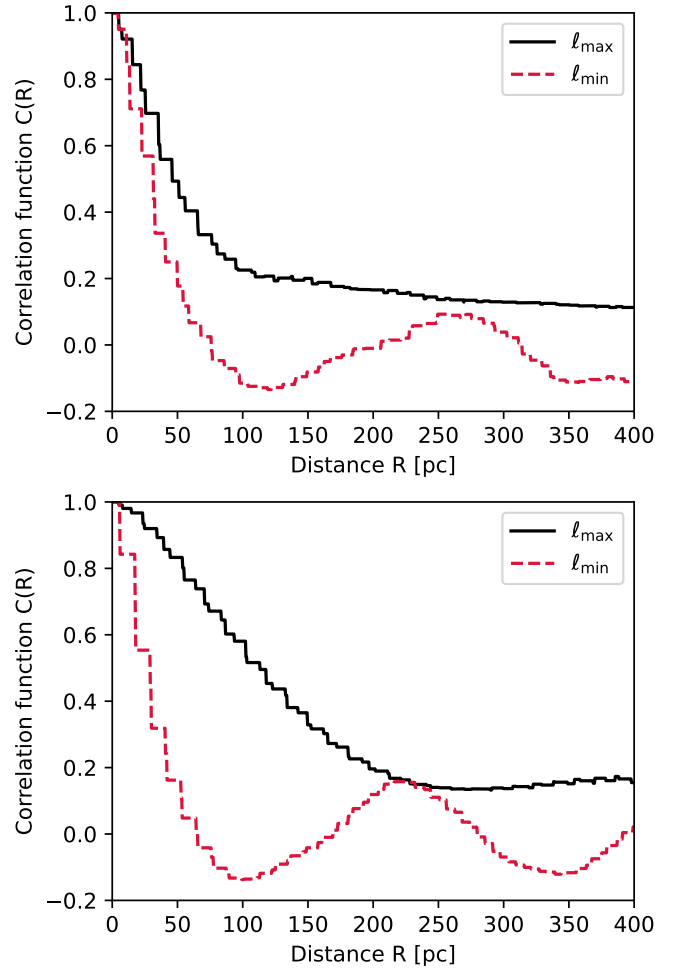


**Figure A2.** Rotation measure correlation function  $C_{RM}$  along the axes of minimal and maximal correlation length displayed in Fig. A1. The RM is computed along the  $z$  axis for Run25 at  $T \approx 1508$  Myr. This time step is in the middle of the dynamical phase. *Top panel:* Mod1 is used, the thermal electron density is proportional to the ISM density. *Bottom panel:* Mod2 is used, the thermal electron density is constant across the box.

		Run25	Run50	Run100
$\ell_{\min}$ [pc]	Mod1	$224 \pm 16$	$235 \pm 7$	$158 \pm 10$
	Mod2	$355 \pm 2$	$345 \pm 4$	$262 \pm 7$
$\ell_{\max}$ [pc]	Mod1	$355 \pm 11$	$330 \pm 4$	$228 \pm 11$
	Mod2	$378 \pm 5$	$364 \pm 2$	$307 \pm 5$

**Table B2.** Comparison for  $RM_y$  of the time average over the last 500 Myr of each run of the minimum correlation length ( $\ell_{\min}$ ) and the maximum one ( $\ell_{\max}$ ) for the two models and the three simulation data sets. The errors are taken as one standard deviation of the distribution.



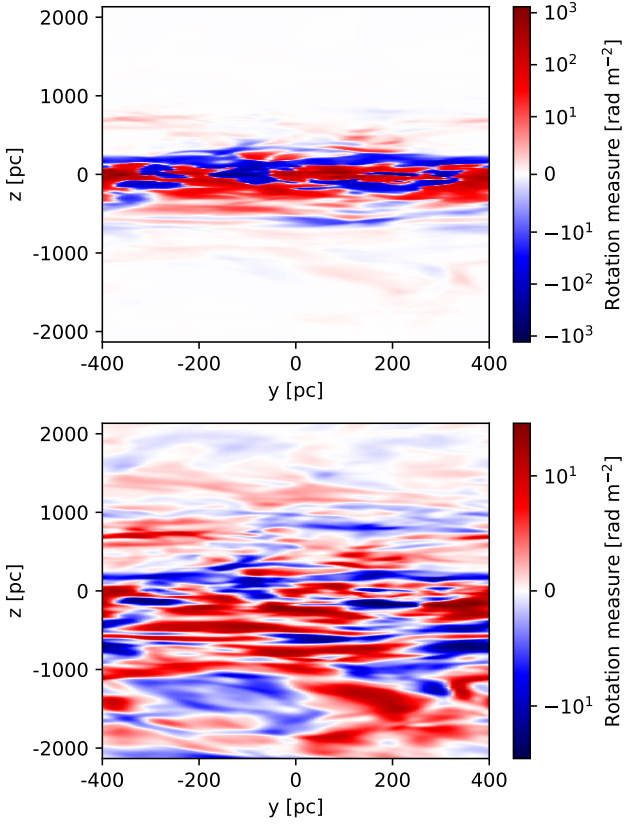


**Figure B1.** Rotation measure along the  $x$  axis for Run25 at  $T \approx 1508$  Myr. This time step is in the middle of the dynamical phase. *Top panel:* Mod1 is used, the thermal electron density is proportional to the ISM density. *Bottom panel:* Mod2 is used, the thermal electron density is constant across the box.

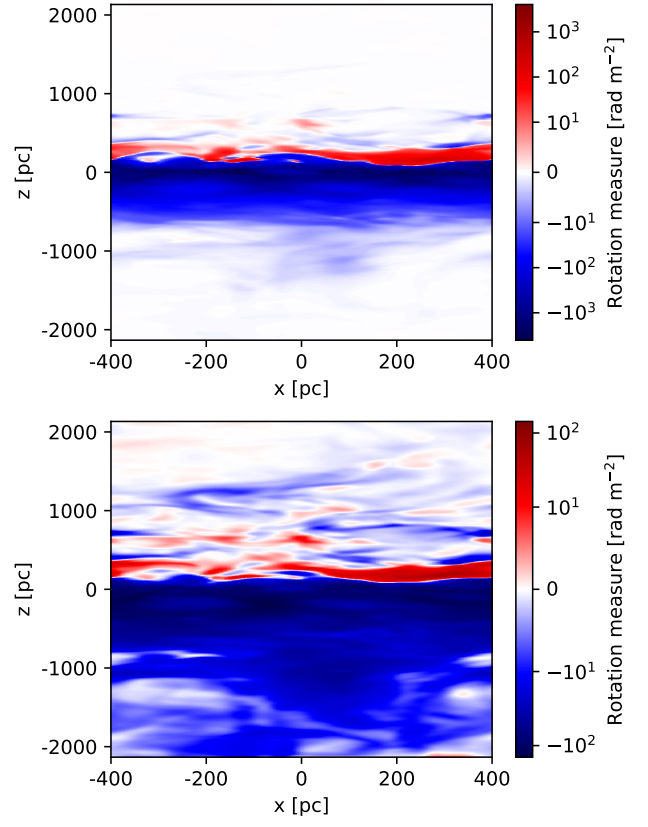


**Figure B2.** Rotation measure along the  $y$  axis for Run25 at  $T \approx 1508$  Myr. *Top panel:* Mod1 is used, the thermal electron density is proportional to the ISM density. *Bottom panel:* Mod2 is used, the thermal electron density is constant across the box.

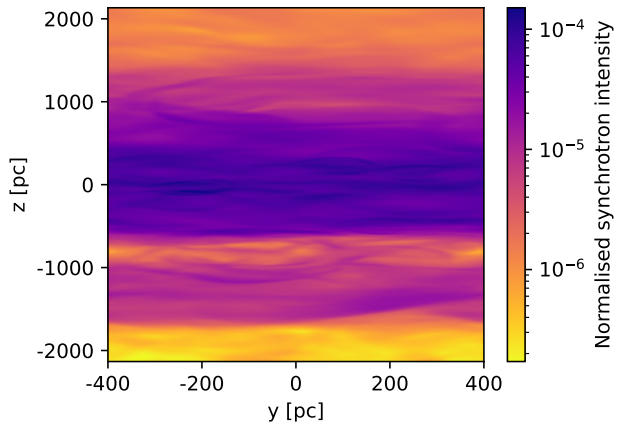
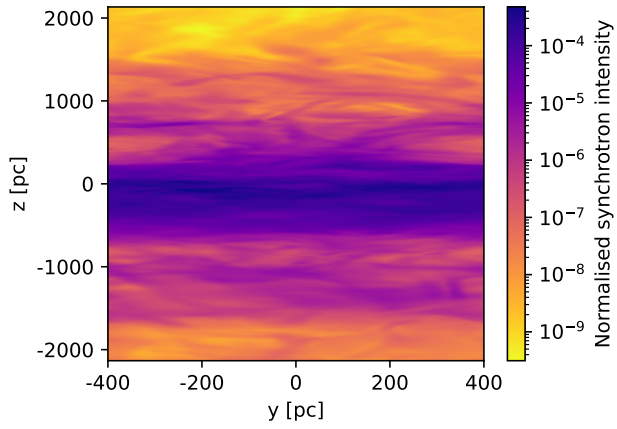


**Figure B3.** Normalised synchrotron radiation intensity along the  $x$  axis for Run25 at  $T \approx 1508$  Myr. This time is in the middle of the dynamical phase. *Top panel:* CRMod1 is used, which is based on equipartition between CR and magnetic energy. *Bottom panel:* CRMod2 is used, in which the CR electrons density is constant across the box.

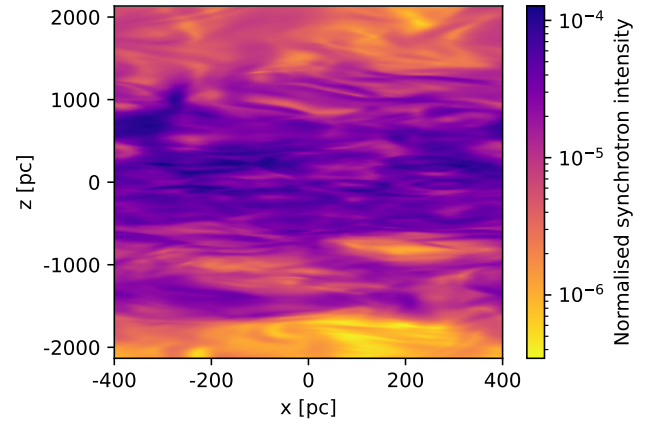
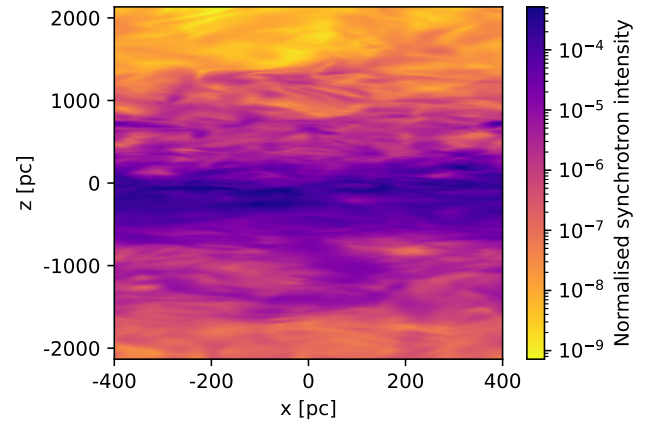


**Figure B4.** Normalised synchrotron radiation intensity along the  $y$  axis for Run25 at  $T \approx 1508$  Myr. This time is in the middle of the dynamical phase. *Top panel:* CRMod1 is used, which is based on equipartition between CR and magnetic energy. *Bottom panel:* CRMod2 is used, in which the CR electrons density is constant across the box.

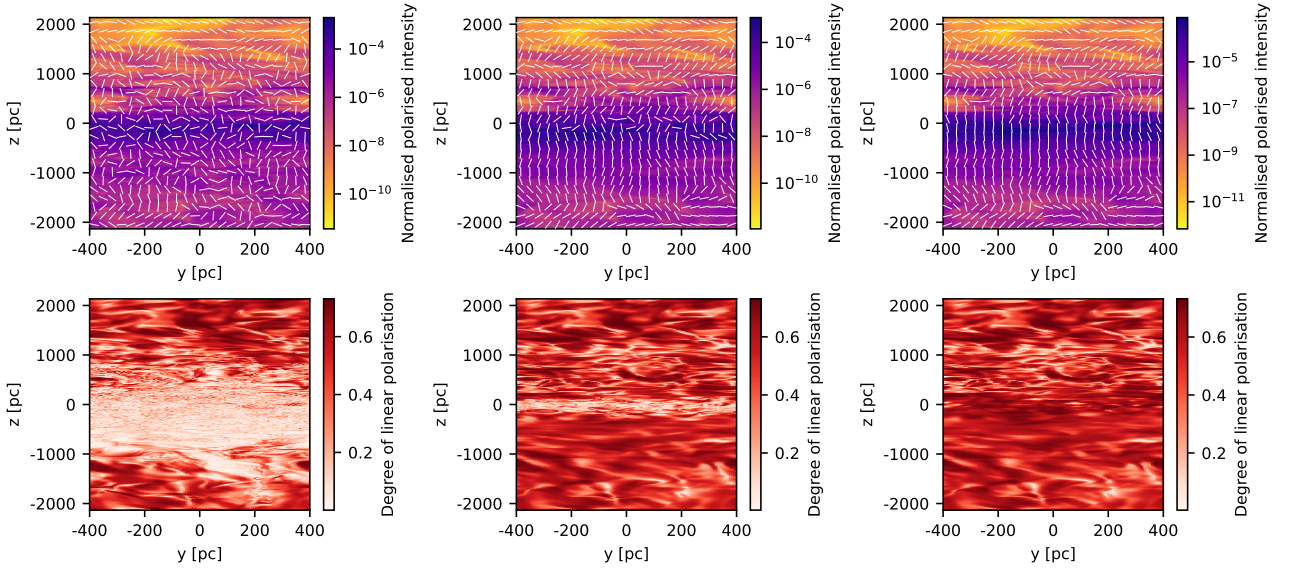


**Figure B5.** *First row:* Normalised polarised intensity maps  $PI_x$  with respect to the  $x$  axis. The lines indicate the observed angle of polarisation  $\Gamma_x$  with respect to the  $x$  axis. *Second row:* Degree of linear polarisation  $p_x$  with respect to the  $x$  axis. The three columns correspond, respectively, to a frequency of observation of 70 MHz, 1.4 GHz, and 5 GHz for Run25 at  $T \simeq 1508$  Myr, i.e. in the dynamical phase. We used Mod1 and CRMod1 to compute all the presented quantities.

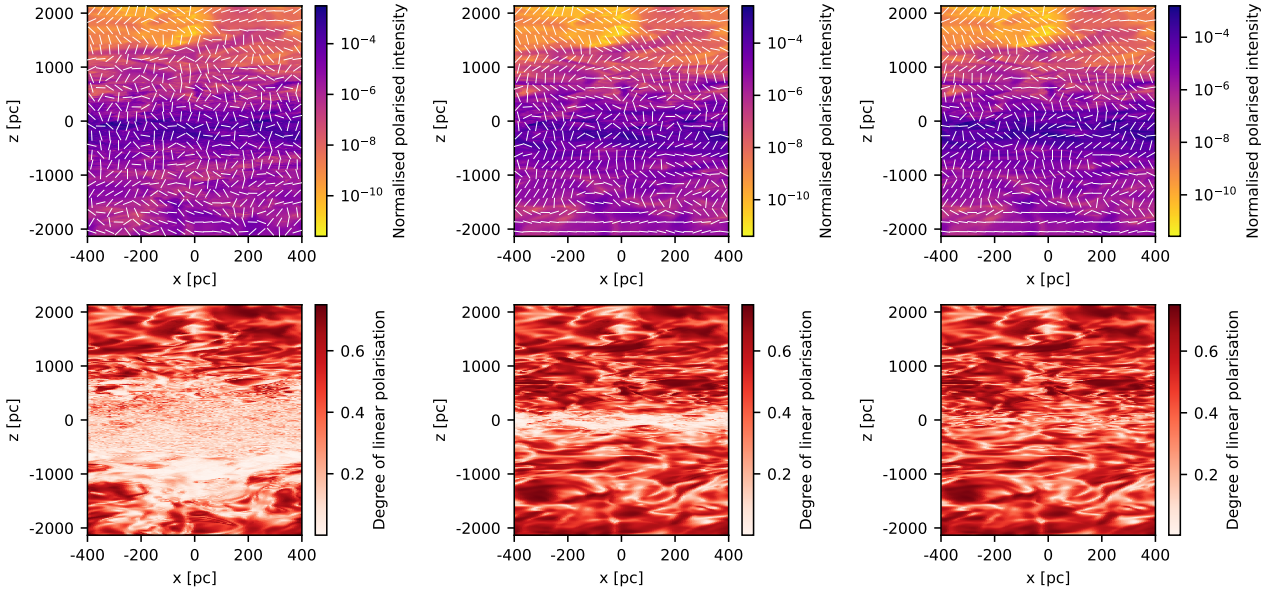


**Figure B6.** *First row:* Normalised polarised intensity maps  $PI_y$  with respect to the  $y$  axis. The lines indicate the observed angle of polarisation  $\Gamma_y$  with respect to the  $y$  axis. *Second row:* Degree of linear polarisation  $p_y$  with respect to the  $y$  axis. The three columns correspond, respectively, to a frequency of observation of 70 MHz, 1.4 GHz, and 5 GHz for Run25 at  $T \simeq 1508$  Myr, i.e. in the dynamical phase. We used Mod1 and CRMod1 to compute all the presented quantities.